

Coercivity Improvement in Ce-Containing (Nd,Pr)-Fe-B-Based Sintered Magnets by Application of the 2-Powder Method

Chi-Chia Lin,* Konrad Opelt, Jürgen Dieter Rossa, Fernando Maccari, Songhak Yoon, Jürgen Gassmann, and Oliver Gutfleisch

The 2-powder method is an effective strategy for enhancing the utilization efficiency of rare earth elements in Nd-Fe-B-based magnets. It involves blending a main powder (MP) with a finer-sized powder characterized by a higher anisotropy field (termed anisotropy powder, AP), producing magnets with core-shell structures. This method overcomes the limitations of the grain boundary diffusion process on magnet dimensions and avoids processing costs associated with additional coating and heating. Herein, the 2-powder method is applied to counteract coercivity and remanence loss in Ce-containing (Nd,Pr)-Fe-B magnets, achieving sustainable gap magnets with reduced criticality. Two types of anisotropy powders: Nd₂Fe₁₄B-based and (Nd,Pr,Dy)₂Fe₁₄B-based, are each blended with the (Ce,Nd,Pr)₂Fe₁₄B-based MP in a 3:7 weight ratio. The MP has a mean particle size of $\approx 4 \mu\text{m}$ and APs of around $2.5 \mu\text{m}$. Compared to the magnet produced from the MP alone, incorporating Nd-enriched and Dy-enriched APs increased coercivity from 750 to 931 and 1362 kA m⁻¹, respectively. The significant improvements are attributable to the formation of core-shell structures, where Nd and Dy are selectively enriched in the shell region of RE₂Fe₁₄B grains. These distribution trends underscore the efficient rare earth element utilization realized through the 2-powder method.

applications, including motors, wind turbines, hybrid electric vehicles, and consumer electronics.^[1] Regarding their high performance, global consumption of Nd-Fe-B magnets reached 164 000 tons in 2022, with projections estimating an increase to 231 000 tons by 2032.^[2] This growing demand accelerates the need for the resource of critical rare earth elements (REs) such as Nd, Pr, and Dy.^[1,3] Figure 1 illustrates that annual global consumption of Nd, Pr, and Dy sources has been exceeding available supplies.^[4] Associated with the increasing demand, concerns surrounding price volatility, resource sustainability, and environmental impact are pressing issues that require immediate attention. Concurrently, the surplus of Ce is coupled with the escalating demands for Nd, Pr, and Dy, leading to an imbalance in the supply and demand of different REs.^[5,6] Incorporating abundant and “free” Ce into Nd-Fe-B magnets offers a solution to these issues and provides an opportunity

1. Introduction


Sintered Nd-Fe-B magnets outperform other permanent magnets around room temperature and are widely utilized in various

to develop resource-conserving magnets with commercial potential, so-called gap magnets.^[7,8]

Nevertheless, previous studies on Ce-containing Nd-Fe-B-based magnets have revealed a severe decline in magnetic performance with increasing Ce substitution, which is attributed to the inferior intrinsic properties of the Ce₂Fe₁₄B phase and the associated deterioration in microstructure.^[9,10] In particular, when the ratio of Ce to total RE content (Ce/TRE) exceeds $\approx 25 \text{ wt\%}$, the REFe₂ Laves phase forms.^[8,11–13] The CeFe₂ phase, with a Curie temperature T_c of $-38 \text{ }^\circ\text{C}$, is paramagnetic at room temperature and is thus considered to play a similar role to RE-rich grain boundary phases (GBPs).^[14,15] However, in (Nd,Pr)-Fe-B-based magnets with partial Ce substitution, the Laves phase typically forms as (Ce,Nd,Pr)Fe₂. The inclusion of Nd and Pr can induce a paramagnetic-to-ferromagnetic transition, as evidenced by the Curie temperatures of NdFe₂ ($T_c = 305 \text{ }^\circ\text{C}$) and PrFe₂ ($T_c = 270 \text{ }^\circ\text{C}$).^[16,17] When the REFe₂ phase is ferromagnetic, it disrupts the magnetic isolation between RE₂Fe₁₄B grains. Furthermore, due to its higher melting point compared to conventional RE-rich phases, the REFe₂ phase exhibits poor wettability during post-sintering annealing and tends to accumulate at grain boundary triple junctions.^[18] At the same time, the

C.-C. Lin, K. Opelt, J. D. Rossa, S. Yoon, J. Gassmann
Fraunhofer Research Institution for Materials Recycling and Resource Strategies IWKS
Aschaffenburg Str. 121, 63457 Hanau, Germany
E-mail: chi-chia.lin@iwks.fraunhofer.de

C.-C. Lin, K. Opelt, F. Maccari, O. Gutfleisch
Department of Materials and Geosciences
Functional Materials
TU Darmstadt
Peter-Grünberg-Str. 16, 64287 Darmstadt, Germany

 The ORCID identification number(s) for the author(s) of this article can be found under <https://doi.org/10.1002/adem.202500054>.

© 2025 The Author(s). Advanced Engineering Materials published by Wiley-VCH GmbH. This is an open access article under the terms of the Creative Commons Attribution License, which permits use, distribution and reproduction in any medium, provided the original work is properly cited.

DOI: 10.1002/adem.202500054

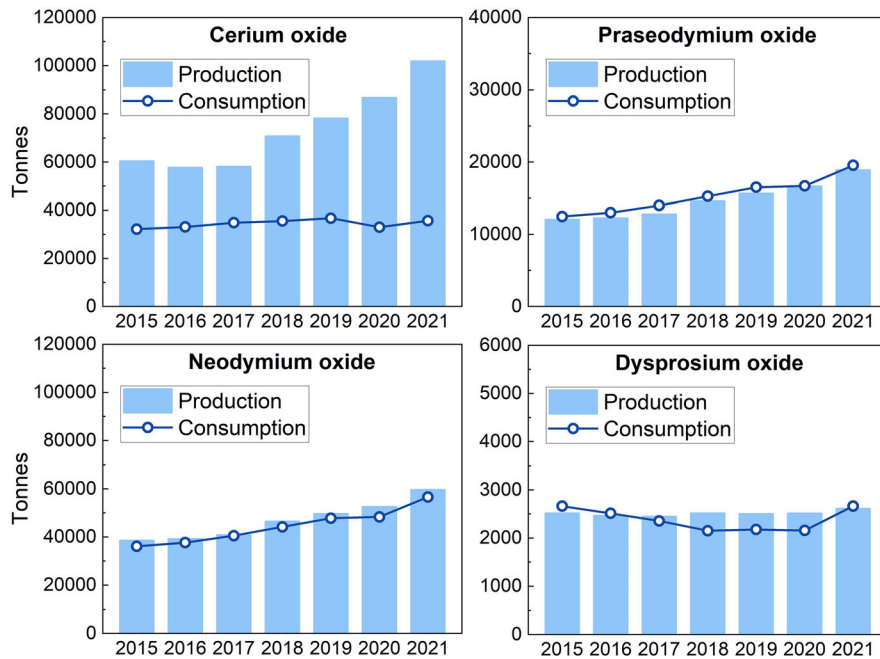


Figure 1. Global production and consumption balance of RE oxides commonly used in Nd-Fe-B-based magnets from 2015 to 2021, based on the 2022 Q2 report by Adamas Intelligence.^[4] Reproduced with permission.^[4] Copyright 2025, Adamas Intelligence.

formation of the REFe₂ phase depletes the RE-rich phase, further impacting the microstructure. In Nd-Fe-B-based sintered magnets, coercivity is primarily governed by the nucleation mechanism, where reversed magnetic domains nucleate at the grain boundaries of RE₂Fe₁₄B matrix grains and propagate under an external magnetic field.^[19] It is quantified as the field strength required to reduce the magnetization to zero and is influenced by factors such as temperature and complex microstructural features, particularly at grain boundaries. When GBPs fail to form a continuous layer around RE₂Fe₁₄B grains due to the presence and aggregation of the REFe₂ phase, reversed domains can propagate unhindered.^[20,21] Consequently, the material experiences a degradation in practical coercivity.

Various approaches, including grain boundary restructuring,^[22–26] grain boundary diffusion process,^[27–31] and dual main phase method,^[15,32–36] have been employed to preserve desirable magnetic properties of Ce-containing Nd-Fe-B-based magnets.^[37] These techniques, collectively known as grain boundary engineering, aim to magnetically harden the surface of RE₂Fe₁₄B grains, acknowledging that Nd-Fe-B-based sintered magnets exhibit nucleation-type magnetization reversal.^[19] The nucleation of reverse domains is typically initiated at grain surfaces, where lattice distortion and atomic defects lower the anisotropy field.^[20,38] Accordingly, selectively modifying the surface composition of RE₂Fe₁₄B grains is a more efficient way to impede reversal than increasing the anisotropy field across the entire grain. For instance, in grain boundary restructuring, Nd- or heavy rare earth (HRE)-rich intergranular additive is blended with (Nd,Ce)₂Fe₁₄B-based powder to increase the amount of RE-rich phases.^[22–26] This approach enhances the continuity of the GBPs while simultaneously enriching the outer layer of (Nd,Ce)₂Fe₁₄B grains with Nd or HRE, thereby

improving the coercivity. Whereas the grain boundary diffusion process introduces Nd or HRE by applying source materials to the surface of already-sintered (Nd,Ce)-Fe-B magnets and heat-diffusing them through intergranular phases.^[27–31] By forming a core-shell structure and concentrating Nd or HRE on the magnet surface, where defects are more prevalent, this process significantly improves coercivity. However, this advantage is limited to magnets less than 4–5 mm thick due to a restricted diffusion length, even when the source is coated on both easy surfaces.^[39–41] On the other hand, the dual main phase method utilizes two RE₂Fe₁₄B-based powders, one with and one without Ce, to develop core-shell structures after sintering.^[15,32–36] Magnets produced by this method contain a mix of (Nd, Ce)₂Fe₁₄B grains with an Nd-enriched shell and Nd₂Fe₁₄B grains with a Ce-enriched shell, with the former contributing to coercivity gain.

In this study, the 2-powder method (2PM) is applied in a way that conceptually differs from the methods described above.^[42] The 2PM was originally proposed for HRE addition in Nd-Fe-B magnets by Löwe et al.^[42] Through semi-industrial scale processing, Opelt et al.^[43] validated the method and demonstrated its effectiveness in improving coercivity while preserving remanence by forming a core-shell structure. Building on the knowledge gained from the previous work, this research extends the application of the 2PM to Ce-containing Nd-Fe-B-based magnets. The method involves mixing a coarser main powder (MP) with a finer powder that has a higher anisotropy field (referred to as anisotropy powder, AP), both of which are RE₂Fe₁₄B-based. The key concept is to apply a Ce-containing MP that is 50–100% larger in size than the AP with a higher Nd or Dy content, as illustrated in **Figure 2**.^[42,43] By leveraging the difference in particle size between the two powders, a core-shell structure

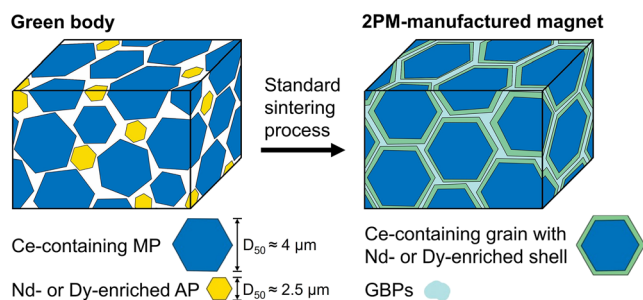


Figure 2. Schematic of the 2PM illustrating the core-shell structure formed after standard sintering process attributed to the designed size difference in the two powders.

featuring an AP-based shell and an MP-based core can be achieved. Specifically, the finer-sized AP is preferentially consumed through the grain growth during the standard sintering process due to its higher surface energy.^[44] As a result, the higher Nd or Dy content in AP is concentrated exclusively in the shell region of $\text{RE}_2\text{Fe}_{14}\text{B}$ grains, effectively enhancing coercivity. Without partial grains exhibiting a Ce-enriched shell like in magnets produced by the dual main phase method, the 2PM demonstrates its potential to enhance coercivity while achieving greater RE utilization efficiency. Furthermore, it retains advantages such as eliminating the need for an additional source-adding step and diffusion heat treatment in the grain boundary diffusion process, making it more cost-effective and less time-consuming. The 2PM also avoids limitations related to magnet shape and size. Moreover, the method is compatible with standard processing routes for Nd-Fe-B sintered magnets, simplifying its integration into commercial mass production.^[43,45] In the present work, Nd-enriched AP₁ and Dy-enriched AP₂ were each blended with the Ce-containing MP. The magnetic properties and microstructures were analyzed and compared to those of the magnet produced solely from MP to assess the effectiveness of the 2PM on Ce-containing Nd-Fe-B sintered magnets. The RE utilization efficiency was evaluated by examining the relationship between magnetic performance and elementary distribution in the core-shell structure.

2. Results and Discussion

2.1. Magnetic Properties

Figure 3 shows demagnetization curves for magnets manufactured with only the MP (MP magnet) and the mixture of 70 wt% MP and 30 wt% AP (AP_{1,2} 2PM magnet), with corresponding densities and magnetic properties detailed in **Table 1**. The densities measured in the 2PM magnets show variations compared to the MP magnet, with the AP₁ 2PM magnet having a slightly lower density of 7.51 g cm^{-3} compared to 7.53 g cm^{-3} in the MP magnet. This reduction is likely attributable to the higher Nd content in the AP₁ 2PM magnet, as the density of the $\text{Nd}_2\text{Fe}_{14}\text{B}$ phase (7.60 g cm^{-3}) is lower than the $\text{Ce}_2\text{Fe}_{14}\text{B}$ phase (7.67 g cm^{-3}).^[9] Conversely, the AP₂ 2PM magnet exhibits a higher density of 7.58 g cm^{-3} due to the additional Dy, considering that $\text{Dy}_2\text{Fe}_{14}\text{B}$ (8.05 g cm^{-3}) is denser than $\text{Ce}_2\text{Fe}_{14}\text{B}$.^[9] Despite these variations, all three magnets exhibit

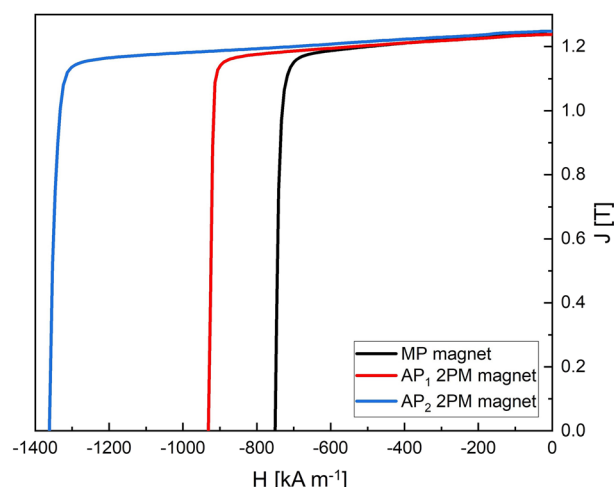


Figure 3. Demagnetization curves of MP, AP₁ 2PM, and AP₂ 2PM magnets. The black curve for the MP magnet overlaps with the blue curve for the AP₂ 2PM magnet in the low-field region. Accurate values of remanence and coercivity are provided in Table 1.

Table 1. Density and magnetic properties of MP, AP₁ 2PM, and AP₂ 2PM magnets.

Magnet	Density ρ [g cm^{-3}]	Remanence B_r [T]	Coercivity H_c [kA m^{-1}]	Energy product $(BH)_{\text{max}}$ [kJ m^{-3}]	Squareness SQ [%]
MP magnet	7.53	1.25	750	288	95
AP ₁ 2PM magnet	7.51	1.24	931	289	98
AP ₂ 2PM magnet	7.58	1.25	1362	295	96

densities aligned with their theoretical fully dense counterparts at similar levels. Comparing the MP magnet with the AP₁ 2PM magnet, the latter exhibits a coercivity of 931 kA m^{-1} , marking a 25% increase over the 750 kA m^{-1} observed in the former. The improvement is consistent with the higher anisotropy field of the $\text{Nd}_2\text{Fe}_{14}\text{B}$ phase (5809 kA m^{-1}) compared to the $\text{Ce}_2\text{Fe}_{14}\text{B}$ phase (2069 kA m^{-1}).^[9] Based on the anisotropy field alone, the additional Nd would be expected to increase coercivity by $\approx 10\%$.^[46,47] Thus, it is deduced that the greater-than-expected improvement in coercivity is governed by the core-shell structure, where concentrated Nd in the grain shell particularly strengthens regions prone to magnetization reversal. The coercivity of 931 kA m^{-1} achieved in the AP₁ 2PM magnet, with a Ce/TRE of 23 wt%, is evaluated in comparison to results from various groups.^[15,27,32–34] As shown in **Figure 4**, for Ce/TRE in the range of 20–30 wt%, the efficiency of the 2PM method for improving coercivity is comparable to that of the dual main phase method and superior to the conventional single powder method. Both the 2PM and the dual main phase method aim to enhance coercivity by mixing two powders with different compositions to form a core-shell structure. While the 2PM develops only an

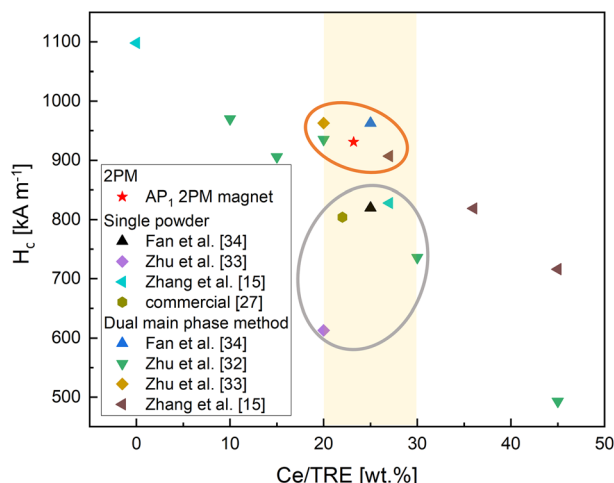


Figure 4. Comparison of coercivity with respect to the Ce/TRE for the AP₁ 2PM magnet and magnets from various research groups.^[15,27,32–34]

Nd-enriched shell through using powders of different sizes, the dual main phase method also forms a Ce-enriched shell. Accordingly, the 2PM is expected to improve coercivity more efficiently. Nevertheless, the coercivity of the AP₁ 2PM magnet remains within the range achieved by the dual main phase method. The absence of continuously distributed GBPs and the development of the RE_{1+ε}Fe₄B₄ phase, as discussed in the next section, provide insight into this observation. With an optimized alloy design, further improvements in coercivity are anticipated in future studies. In contrast, the remanence of the AP₁ 2PM magnet slightly decreases from 1.25 T for the MP magnet to 1.24 T, despite the Nd₂Fe₁₄B phase having a higher saturation magnetization (1.60 T) than the Ce₂Fe₁₄B phase (1.17 T).^[9] The remanence loss indicates the development of a secondary soft magnetic phase, which is proved to be RE_{1+ε}Fe₄B₄ by the microstructure. Detailed analysis will be discussed in Section 2.2. For the AP₂

2PM magnet, an extraordinary 81% increase in coercivity compared to the MP magnet is observed, reaching 1362 kA m⁻¹. This enhancement is intrinsically attributed to the high anisotropy field of 11 937 kA m⁻¹ for the Dy₂Fe₁₄B phase, facilitated by the incorporation of 3 wt% Dy.^[9] Similar to the AP₁ 2PM magnet, the core-shell structure effectively promotes magnetic hardening at the RE₂Fe₁₄B grain surfaces, contributing to the significant coercivity gain. Remarkably, the remanence of the AP₂ 2PM magnet remains consistent at 1.25 T, although the Dy₂Fe₁₄B phase exhibits a lower saturation magnetization (0.71 T) than Ce₂Fe₁₄B.^[9] The fact suggests a preferential substitution of Dy for Ce rather than for Nd or Pr, along with a diminishment of the REFe₂ phase. In comparison, Yan et al.^[10] produced a Ce-containing magnet with a Dy content of 3 wt% and a Ce/TRE of 21.6 wt%, which is similar to the composition of the AP₂ 2PM magnet in this study. This magnet, produced using a single powder, reaches a remanence of 1.24 T and a coercivity of 1331 kA m⁻¹. Notably, the 2PM-manufactured magnet demonstrates enhanced magnetic properties, even with a slightly higher Ce content, indicating a superior RE utilization efficiency. Both 2PM magnets show improved squareness, indicating a reduced REFe₂ phase and a rather homogeneous core-shell structure achieved throughout the entire magnets. To verify the homogenization of the core-shell structure within the magnets, samples were tested at their original thickness after production and at different cut thicknesses. The demagnetization curves measured at various thicknesses are highly consistent, supporting a uniform distribution of the core-shell structure. The associated data can be found in the Supporting Information.

In addition to room-temperature performance, the magnets were examined at elevated temperatures ranging from 80 °C to 180 °C in 20 °C intervals. **Figure 5** demonstrates the temperature-dependent remanence and coercivity for the three magnets. Corresponding temperature coefficients α and β are calculated by

$$\alpha = \frac{B_{r_2, T_2} - B_{r_1, T_1}}{B_{r_1, T_1} \times (T_2 - T_1)} \times 100\% \quad (1)$$

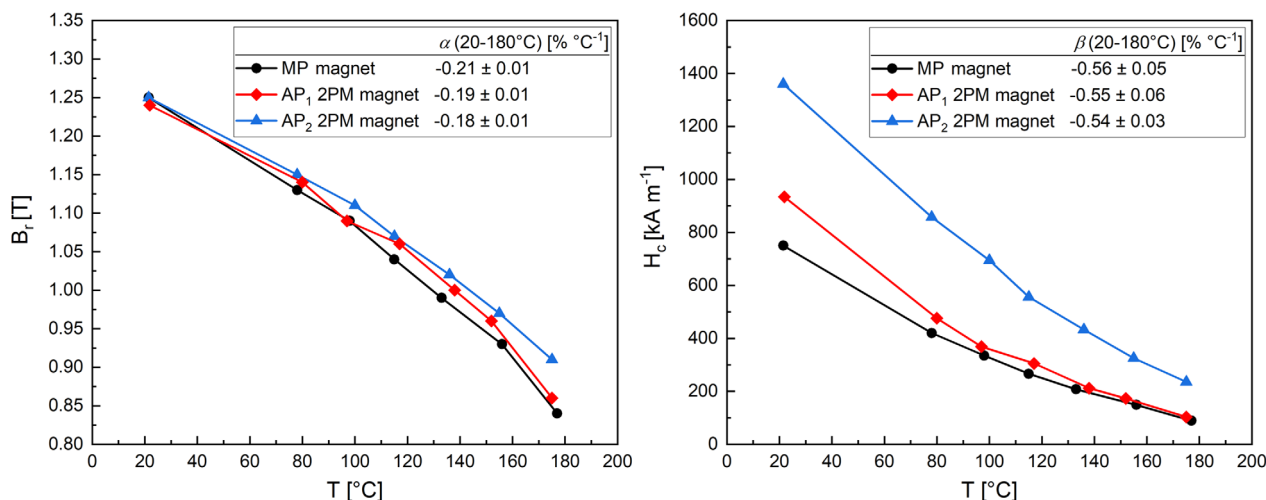


Figure 5. Temperature dependence of remanence and coercivity for MP and 2PM magnets measured from room temperature to 180 °C. The calculated temperature coefficients α and β for remanence and coercivity are displayed alongside the curves.

and

$$\beta = \frac{H_{c_2, T_2} - H_{c_1, T_1}}{H_{c_1, T_1} \times (T_2 - T_1)} \times 100\% \quad (2)$$

Although all magnets suffer considerable thermal degradation in magnetic properties, the 2PM-manufactured ones maintain their advantages at high temperatures. The $|\alpha|$ value decreases with increasing Nd and Dy contents, consistent with the trend of a lower drop in saturation magnetization for the $\text{Nd}_2\text{Fe}_{14}\text{B}$ phase compared to the $\text{Ce}_2\text{Fe}_{14}\text{B}$ phase, and with the instead increment of saturation magnetization of $\text{Dy}_2\text{Fe}_{14}\text{B}$ as the temperature rises from 20 to 180 °C.^[48] Meanwhile, the MP magnet and AP₁ 2PM magnet exhibit similar $|\beta|$ values, corresponding to the comparable dependence of the anisotropy field within this temperature range for $\text{Nd}_2\text{Fe}_{14}\text{B}$ and $\text{Ce}_2\text{Fe}_{14}\text{B}$.^[48] In contrast, the incorporation of Dy results in a slight decrease in $|\beta|$, denoting the higher temperature stability of the anisotropy field for $\text{Dy}_2\text{Fe}_{14}\text{B}$.

To further investigate the Curie transformations of the $\text{RE}_2\text{Fe}_{14}\text{B}$ and REFe_2 phases, the thermal behavior of the magnetic moment was analyzed using vibrating sample magnetometer (VSM). In **Figure 6**, sharp peaks corresponding to the Curie temperatures of the $\text{RE}_2\text{Fe}_{14}\text{B}$ phases were identified by the first derivative of the magnetic moment with respect to temperature. The Curie temperatures determined for MP, AP₁ 2PM, and AP₂ 2PM magnets are 270, 282, and 287 °C, respectively. The increased Curie temperatures in the two 2PM-manufactured magnets are consistent with their better retained magnetic performance at tested temperatures up to 180 °C. In contrast, no transition temperature related to the REFe_2 phase was observed in the temperature-dependent magnetization curves. Given that the REFe_2 phase constitutes a minor proportion of less than 1% of the overall magnet, measuring its Curie temperature is challenging. Therefore, the Curie temperature of the REFe_2 phase can only be inferred to be above room temperature based on the ratios of different REs detected by energy-dispersive X-ray spectroscopy (EDX).

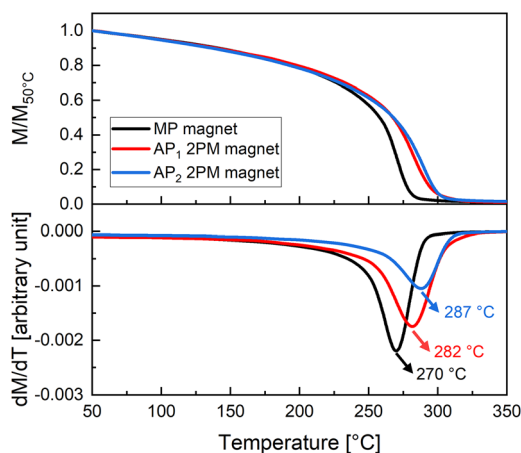


Figure 6. Temperature dependence of the magnetization M that is normalized to the magnetization at 50 °C $M_{50\text{ °C}}$ with an applied magnetic field of 1000 Oe (80 kA m^{-1}), along with the corresponding first derivative dM/dT . The marked temperatures indicate the Curie temperatures of the $\text{RE}_2\text{Fe}_{14}\text{B}$ phases.

2.2. Microstructure and Elemental Distribution

To interpret the changes in magnetic properties induced by the 2PM, microstructures and compositions of each phase are studied by scanning electron microscope (SEM) and EDX, as shown in **Figure 7** and **Table 2**. Table 2 shows that the REFe_2 phases in all three magnets contain certain amounts of Nd and Pr. As discussed previously, the Curie temperature of the REFe_2 phase is critically dependent on the RE components. In this study, the quantities of REFe_2 phases in the samples are too small to allow for qualitative characterization of their Curie temperatures through temperature-dependent magnetization measurements. Tang et al. demonstrated that the Curie temperature is above room temperature for $(\text{Nd}_{1-x}\text{Ce}_x)\text{Fe}_2$ when $x < 0.8$ and for $(\text{Pr}_{1-x}\text{Ce}_x)\text{Fe}_2$ when $x < 0.9$.^[17,49] Here, the REFe_2 phases all exhibit Ce/TRE below 0.8, indicating that they are soft ferromagnetic at room temperature, which negatively affects both remanence and coercivity. Although the amount of the REFe_2 phase is small in the magnets, it can severely decrease the coercivity, since it simultaneously reduces the continuity of the GBPs. Figure 7 reveals the presence of the REFe_2 phase and inadequate wetting of RE-rich GBPs in the MP magnet, which leads to ineffective exchange decoupling of $\text{RE}_2\text{Fe}_{14}\text{B}$ grains and the corresponding low coercivity of 750 kA m^{-1} in the demagnetization curve. The AP₁ 2PM magnet, with additional Nd introduced by AP₁, demonstrates a reduced area fraction of the REFe_2 phase. An unusual finding is the notably high Nd content in the REFe_2 phase of the AP₁ 2PM magnet, while Ce typically has a higher affinity for the REFe_2 phase due to the stabilizing effect of its 4f electron. The underlying cause remains unclear, as there is limited understanding of the REFe_2 phase composition in Nd-Fe-B-based magnets with varying levels of Ce substitution, necessitating further investigation. Although the REFe_2 phase is reduced, the expected improvement in GBP wettability is not observed. The formation of the $\text{RE}_{1+e}\text{Fe}_4\text{B}_4$ phase is probably the reason, which is also identified as the primary cause of the remanence loss and the relatively modest gain in coercivity compared to the AP₂ 2PM magnet. To understand the formation of the $\text{RE}_{1+e}\text{Fe}_4\text{B}_4$ phase in the AP₁ 2PM magnet, the chemical composition was analyzed using ICP-OES. As shown in **Table 3**, the measured concentrations of all REs align closely with the designed composition. In contrast, the transition metals (TMs), including Al, Cu, and Ga, exhibit notable deviations. Since these TM additives constitute a tiny proportion of the magnet, variations in the major elements can result in relatively high measurement errors for these minor components. In view of the similar amounts of TMs measured in all three magnets, the observed deviations are primarily attributed to measurement errors. In the AP₁ 2PM magnet, shifts in the contents of Co and B were observed, indicating that composition changes occur during the powder metallurgy process of AP₁. The slight excess of B in the AP₁ 2PM magnet likely drives the formation of the $\text{RE}_{1+e}\text{Fe}_4\text{B}_4$ phase. Since secondary phases such as REFe_2 are involved in Ce-containing magnets, the phase composition can be further susceptible to the small shift of B amount than in conventional Nd-Fe-B magnets. Given the large-scale production of powder batches (several kilograms), a repetition of the production process was not conducted. The composition shift could originate from various stages of the

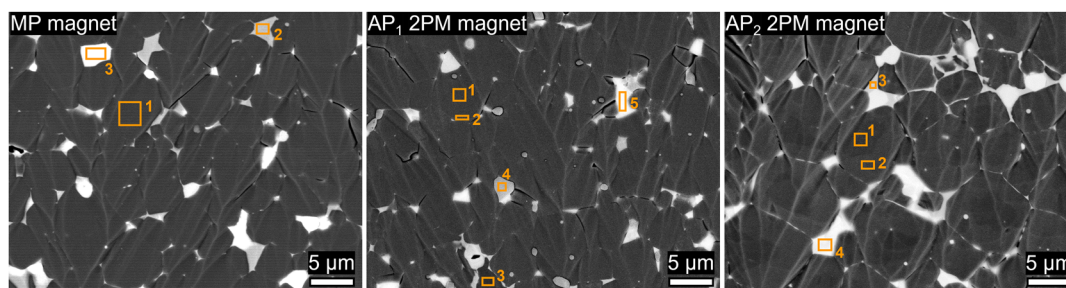


Figure 7. SEM BSE images of MP, AP₁ 2PM, and AP₂ 2PM magnets. The bright topographical lines in the images are preparation line artifacts introduced by triple ion beam polishing, not defects or scratches. The average grain sizes, determined using the intercept method, are 3.8, 3.8, and 4.4 μm for the MP, AP₁ 2PM, and AP₂ 2PM magnets, respectively. It is important to note that the grain sizes calculated by this method may underestimate the actual values, as the sample cross-section does not always bisect the grains at their center. The observed distinct phases are marked and analyzed by EDX, with results listed in Table 2.

Table 2. The elemental composition of the phases marked in Figure 7 for MP, AP₁ 2PM, and AP₂ 2PM magnets received from EDX spectra. Contents of Co and TM elements are not included, therefore the total may be less than 100 wt%.

MP magnet		Elemental composition [wt%]						
Phase	Nd	Pr	Ce	Dy	Fe	B	O	
1. RE ₂ Fe ₁₄ B	14.3	4.7	9.8	–	71.0	–	–	
2. REFe ₂	9.3	3.5	43.5	–	43.7	–	–	
3. RE-rich	48.0	17.9	23.3	–	5.2	–	5.6	
AP ₁ 2PM magnet								
1. RE ₂ Fe ₁₄ B (core region)	15.1	4.9	8.9	–	70.5	–	–	
2. RE ₂ Fe ₁₄ B (shell region)	19.9	3.2	6.2	–	70.3	–	–	
3. RE _{1+e} Fe ₄ B ₄	26.1	3.5	7.9	–	52.8	9.7	–	
4. REFe ₂	34.0	7.2	12.0	–	44.7	–	–	
5. RE-rich	57.1	13.2	19.2	–	5.0	–	5.6	
AP ₂ 2PM magnet								
1. RE ₂ Fe ₁₄ B (core region)	14.7	5.1	9.1	–	71.1	–	–	
2. RE ₂ Fe ₁₄ B (shell region)	14.8	4.8	6.1	3.6	70.7	–	–	
3. REFe ₂	12.1	3.5	40.2	–	44.3	–	–	
4. RE-rich	43.3	25.9	21.2	–	8.4	–	1.2	

powder metallurgy process, each requiring extensive optimization. Considering that this study is focused on evaluating the feasibility of applying the 2PM to Ce-containing magnets, the observed compositional variations were deemed acceptable within the scope of this research. For the Nd-enriched AP₁

2PM magnet, identifying a core-shell structure in the SEM back-scattered electron (BSE) image is challenging due to the close atomic numbers of light REs. EDX elemental mapping is thus performed, revealing RE₂Fe₁₄B grains with Nd-enriched shells, as demonstrated in Figure 8. The EDX line scan across selected grains of the AP₁ 2PM magnet in Figure 9 provides additional insight into RE distribution within the core-shell structure. The substitution of Ce and Pr by Nd is clearly observed at the surface area of RE₂Fe₁₄B grains, which confirms the formation of a core-shell structure. However, the core-shell structure is not uniformly developed. The mean grain sizes of the AP₁ 2PM magnet and the MP magnet are comparable, each measuring around 3.8 μm. Since the formation of the core-shell structure based on the 2PM relies on adequate grain growth during sintering, the limited grain size development observed in the AP₁ 2PM magnet explains the relatively inhomogeneous distribution of the core-shell structure throughout the magnet. Therefore, the efficiency of coercivity enhancement is lower than in the AP₂ 2PM magnet. Future studies should focus on precise control of the chemical composition, optimization of the core-shell structure, and mitigation of the RE_{1+e}Fe₄B₄ phase to improve the efficiency.

Compared to the MP and AP₁ 2PM magnets, the Dy-enriched AP₂ 2PM magnet exhibits a larger mean grain size of 4.4 μm, a diminished REFe₂ phase, and an improved GBP wettability, as shown in Figure 7. The improved continuity of the GBPs is deduced to arise from the depletion of the REFe₂ phase, which increases the proportion of RE-rich phases. All these features contribute to the improved coercivity. Additionally, the core-shell structure is identifiable in the SEM BSE image. The distribution of REs demonstrated in Figure 8 indicates that Dy preferentially substitutes Ce rather than all light REs in the shell region of the RE₂Fe₁₄B grain, which accounts for the significant improvement in coercivity. This tendency also mitigates the expected decrease

Table 3. The designed and measured compositions (in wt%) of MP, AP₁ 2PM, and AP₂ 2PM magnets. The MP and 2PM magnets contain Ce/TRE of 33 and 23 wt%, respectively.

Magnet	Nd	Pr	Ce	Dy	TRE	Fe	Co	TM	B
MP magnet = Nd _{15.1} Pr _{5.1} Ce ₁₀ Fe _{bal.} TM _{0.32} B _{0.91}	14.9	5.2	9.6	–	29.7	Bal.	–	0.51	0.90
AP ₁ 2PM magnet = Nd _{19.6} Pr _{3.6} Ce ₇ Fe _{bal.} Co _{0.57} TM _{0.32} B _{0.91}	20.0	3.9	6.6	–	30.5	Bal.	0.15	0.59	1.00
AP ₂ 2PM magnet = Nd _{15.1} Pr _{5.1} Ce ₇ Dy ₃ Fe _{bal.} Co _{0.57} TM _{0.32} B _{0.91}	15.2	5.5	6.8	2.9	30.4	Bal.	0.59	0.58	0.95

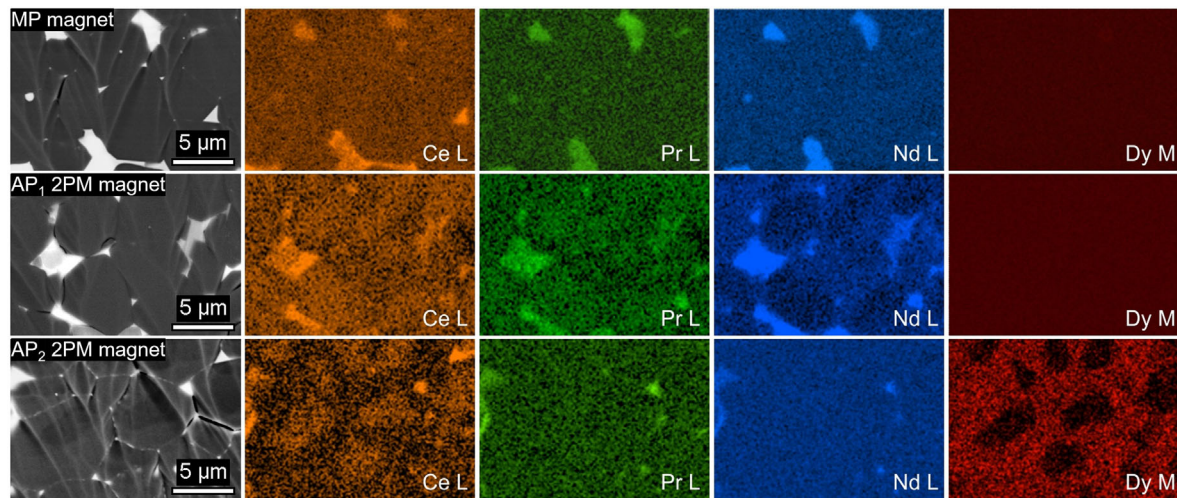


Figure 8. The microstructures with EDX mapping showing Ce, Pr, Nd, and Dy distributions of MP, AP₁ 2PM, and AP₂ 2PM magnets. The absence of Dy signal in MP and AP₁ 2PM magnets confirms that no Dy addition is included in these magnets.

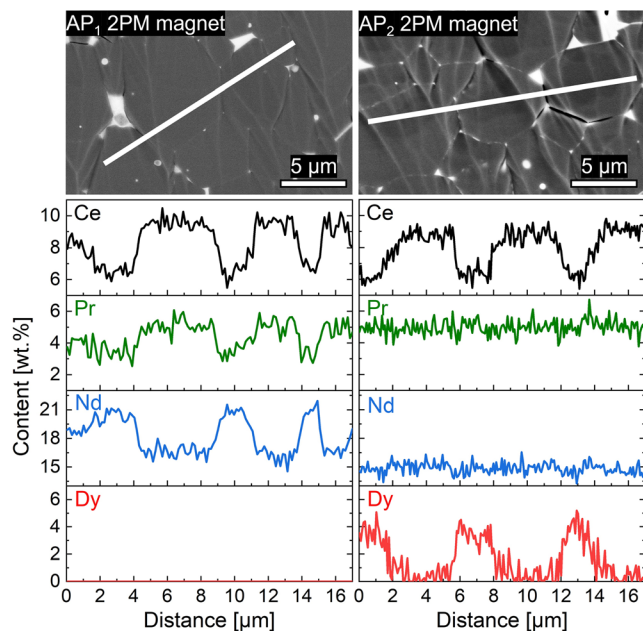


Figure 9. EDX line scans of AP₁ 2PM and AP₂ 2PM magnets. The distribution of Ce, Pr, Nd, and Dy contents along selected line regions is shown.

in remanence typically associated with Dy substitution, as the higher saturation magnetization contributions from Nd and Pr are retained. However, the saturation magnetization of Dy₂Fe₁₄B (0.71 T) remains lower than that of Ce₂Fe₁₄B (1.17 T).^[9] It is thus speculated that the reduced REFe₂ phase in the AP₂ 2PM magnet contributes to the preservation of remanence. As the REFe₂ phase diminishes to a negligible amount, more Fe can enter the RE₂Fe₁₄B phase, thereby compensating for the potential loss in remanence. As shown by the EDX line measurements in Figure 9, the AP₁ 2PM and AP₂ 2PM magnets exhibit similar concentrations of different REs in the grain core,

which are close to those in the MP. Meanwhile, the shell region of the grains presents RE ratios dominated by their respective mixed APs. This observation highlights that the distribution of different REs within the core-shell structure can be controlled by managing the composition of the MP and AP, allowing for optimized RE utilization efficiency in terms of properties and cost.

The measured X-ray diffraction (XRD) patterns, analyzed using Rietveld refinements, are presented in Figure 10. The quantities of phases identified from the diffraction patterns, along with the lattice parameters for the primary RE₂Fe₁₄B phase, are derived from the Rietveld refinement and detailed in Table 4. A comparison between the MP and 2PM magnets reveals an increase in the lattice parameters for the AP₁ 2PM magnet. In contrast, the lattice parameter *a* in the AP₂ 2PM magnet remains comparable to that of the MP magnet, while the parameter *c* exhibits a reduction. The variations are consistent with the principle of lanthanide contraction, along with the replacement of Ce by Nd and Dy in the shell regions of RE₂Fe₁₄B grains in AP₁ and AP₂ 2PM magnets, respectively.^[9] Additionally, the XRD patterns confirm a reduction in the REFe₂ phase within 2PM-manufactured magnets, as evidenced by the diminishing intensity of characteristic REFe₂ peaks and a corresponding decrease in calculated phase quantities. The observation aligns with previous studies indicating that the REFe₂ phase predominantly develops when Ce/TRE exceeds 25 wt%.^[12]

2.3. Magnetic Domain Structures

Kerr microscopy was carried out along the easy magnetization direction of MP and 2PM magnets in a thermally demagnetized state to characterize the magnetic domains and correlate them with the bulk magnetic properties. The dark and bright contrasts observed in Figure 11 correspond to opposing magnetization directions perpendicular to the surface. In all samples, the majority of grains exhibit a star-like domain pattern, typical of materials

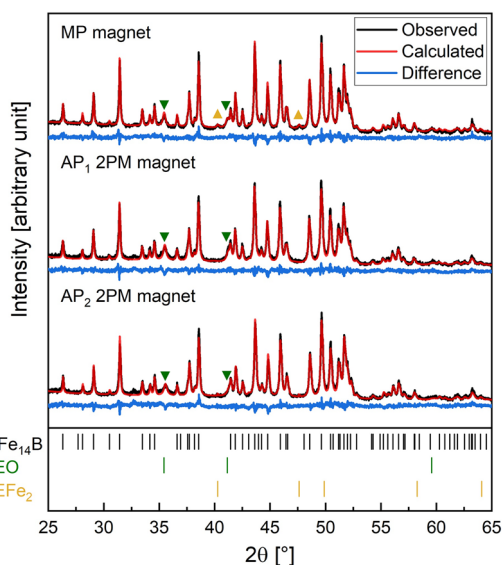


Figure 10. XRD pattern and Rietveld refinement for MP, AP₁ 2PM, and AP₂ 2PM magnets. Yellow equilateral triangles mark the characteristic peaks of the REFe₂ phase, and the green inverted triangles indicate that of REO.

Table 4. Calculated phase contents and lattice parameters of the RE₂Fe₁₄B phase based on the XRD rietveld refinements. The discrepancy values that indicate the quality of the refinement, including *R*-factor *R*_{wp} and goodness of fit χ^2 , are listed.

Magnet	Phase contents [%]			Lattice parameters of RE ₂ Fe ₁₄ B [Å]		Rietveld discrepancy values	
	RE ₂ Fe ₁₄ B	REFe ₂	REO	<i>a</i>	<i>c</i>	<i>R</i> _{wp}	χ^2
MP magnet	96.30	0.74	2.96	8.788	12.188	6.79	2.21
AP ₁ 2PM magnet	94.90	0.20	4.90	8.792	12.196	6.29	1.95
AP ₂ 2PM magnet	95.08	0.07	4.85	8.787	12.175	6.82	2.20

with high magnetocrystalline anisotropy when observed along the easy axis. The observed domain pattern indicates a high degree of texture, consistent with the high remanence and squareness measured in the demagnetization curves. A small fraction of grains show stripe-like domains, revealing misoriented crystals with their easy magnetization axis aligned within the image plane. Combining these observations with the SEM BSE images (Figure 7) of MP and AP₁ 2PM magnets, the lack of continuity in the GBPs leads to magnetic coupling and interaction between adjacent grains. In contrast, the AP₂ 2PM magnet exhibits continuous GBP, indicating enhanced magnetic decoupling. This improvement hinders the propagation of reversed domains across different grains, resulting in higher coercivity. According to domain theory, the surface domain width is proportional to the domain wall energy and the square root of anisotropy energy in uniaxial samples of considerable thickness.^[50,51] The average surface domain width *W* was calculated using the stereological method^[52]

$$W = \frac{2 \times \text{Total test line length}}{\pi \times \text{Number of intersections}} \quad (3)$$

As illustrated in Figure 11, the values are based on nine arbitrary test lines crossing each grain. Differences in the anisotropy fields between the core and shell regions within individual grains are expected to manifest as variations in domain width. In the AP₁ 2PM magnet, the Nd-enriched shells are generally less than 1 μm thick, making it difficult to discern differences in domain structure due to the resolution limitations of Kerr microscopy. In contrast, the AP₂ 2PM magnet demonstrates a distinct core-shell structure with a noticeable shell thickness in the SEM image. The observation highlights significant differences in anisotropy fields between the core and shell regions, attributable to the Dy concentrations. Although not uniformly evident across all grains, likely due to internal surface misalignment, a thickened domain width in the shell region is observed in the grains shown in the lower right of Figure 11. This observation suggests that Dy enrichment in the surface region of grains can locally modulate

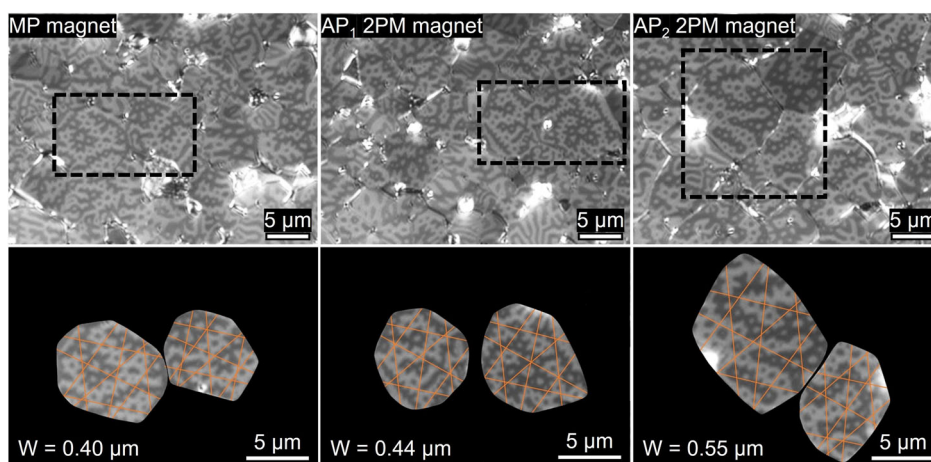


Figure 11. Domain structures observed on cut surfaces perpendicular to the easy-axis of MP, AP₁ 2PM, and AP₂ 2PM magnets based on the polar magneto-optical Kerr effect. Domain widths of two grains with well-aligned star-like patterns of each sample were calculated based on a stereological method with arbitrary test lines demonstrated in the below cutout area. The calculated average domain widths *W* are labeled.

magnetic properties, thereby effectively enhancing magnetic hardness against demagnetization.

3. Conclusion

In this study, the magnetic properties and microstructures of 2PM-manufactured magnets were investigated to evaluate the effectiveness of 2PM in Ce-containing (Nd,Pr)-Fe-B magnets. The demagnetization curves revealed that the incorporation of additional Nd and Dy led to a 25% and 81% increase in coercivity, from 750 to 931 and 1362 kA m⁻¹, respectively. The enhanced coercivity observed in the 2PM-manufactured magnets is attributed to the higher anisotropy field of the introduced APs, along with the contributions from the core-shell structure suggesting an efficient magnetic hardening effect at the grain surfaces. This core-shell effect enables the HRE-free AP₁ 2PM magnet with 23 wt% Ce/TRE replacement to achieve a commercial grade of N38,^[4] while reducing the cost of RE raw materials by 22% compared to conventional Nd-Fe-B magnets.^[53] Microstructural analysis confirms the formation of core-shell structures in both 2PM-manufactured magnets. A comparison of RE distributions in the core-shell structures of Nd-enriched AP₁ 2PM and Dy-enriched AP₂ 2PM magnets revealed that the RE contents in the shell region of RE₂Fe₁₄B grains are primarily determined by the AP composition. The preferential distribution of Nd and Dy in the shell region accounts for the more effective coercivity gain achieved in the 2PM magnets. This observation demonstrates the control of the 2PM over RE distribution in the core-shell structure and highlights the potential to enhance RE utilization by optimizing the compositions of the two powders. In conclusion, 2PM has been identified as a promising approach to enhance coercivity in Ce-containing (Nd,Pr)-Fe-B magnets through the formation of core-shell structures, thereby increasing their commercial viability. Conceptually distinct from other techniques, the 2PM evenly distributes sources with higher anisotropy fields throughout the magnet, eliminating limitations related to magnet dimensions. Consequently, this method is particularly suitable for applications involving large-size magnets that the grain boundary diffusion process cannot address. Moreover, the 2PM integrates seamlessly into the traditional manufacturing process, requiring no extra steps. This makes it a more time- and cost-efficient alternative. Building on the insights into RE distribution gained in this study, future research should prioritize optimizing the RE contents in both the MP and AP to further improve the magnetic performance while minimizing the use of more critical REs.

4. Experimental Section

The chemical compositions for MP, AP₁, and AP₂ were designed as Nd_{15.1}Pr_{5.1}Ce₁₀Fe_{bal}TM_{0.32}B_{0.91}, Nd_{30.2}Fe_{bal}Co_{1.9}TM_{0.32}B_{0.91}, and Nd_{15.1}Pr_{5.1}Dy₁₀Fe_{bal}Co_{1.9}TM_{0.32}B_{0.91}, respectively. The didymium-based compounds, containing Nd and Pr in their natural 3:1 ratio as found in RE ores, were adopted to avoid the complex, costly, and environmentally harmful separation process of Nd and Pr. Alloys with the designed compositions were prepared using an induction melter (VISA 15, SYSTEC) for the MP and a strip caster (Magcaster-50, ULVAC) for the APs. These alloys were exposed to a hydrogen deprecipitation process in a 20 L chamber (FCT Anlagenbau GmbH) under a 3-bar hydrogen atmosphere into coarse particles. The particles were then milled by a target jet mill (MJQ Lab, Hosokawa Alpine AG) using nitrogen as the carrier gas to produce fine powders with diameters D₅₀ of 3.9, 2.4, and 2.6 μm for MP, AP₁, and

AP₂, respectively. The detailed particle size distribution and the contents of oxygen, nitrogen, and hydrogen in the jet-milled powders can be found in the Supporting Information. For the 2PM magnets, a blend of 70 wt% MP and 30 wt% AP was mixed using a mixer mill (MM 400, Retsch). A sample of the powder weighing 5.5 g was aligned under a magnetic field of 2.6 T and consolidated into a green body using a transverse field pressing method. Afterward, the green body wrapped in molybdenum foil was sintered at temperatures ranging from 1020 to 1060 °C, depending on the mixture, and then annealed in two steps at 900 and 500 °C in a vacuum tube furnace. Each heat treatment was followed by water quenching. Finally, the oxidized surface was ground off, producing magnets with dimensions of ≈12 × 10 × 6 mm³.

The particle size distributions of the jet-milled powders were measured by laser diffraction (Mastersizer 3000, Malvern). The oxygen, nitrogen, and hydrogen contents were analyzed using an inert gas melting process (ONH 836 analyzer, Leco), and the chemical composition was determined by inductively coupled plasma optical emission spectrometry (ICP-OES, OPTIMA 8300 DV, PerkinElmer LAS GmbH). The demagnetization curves and magnetic properties of the sintered magnets at elevated temperatures were measured using a hysteresisgraph (Permagraph, Magnet-Physik Dr. Steingroever GmbH). Temperature-dependent magnetization curves were measured by a VSM (LakeShore). The surfaces of the sintered magnets oriented toward the easy axis were finely prepared using a triple ion beam cutter (TIC 3x, Leica), and the microstructure was examined with a field emission SEM (FE-SEM, Merlin, Carl Zeiss Microscopy Ltd.) equipped with a BSE detector. The ion beam polishing technique produces high-quality surfaces for observing core-shell structures, while it can introduce preparation line artifacts. In addition to BSE imaging, compositional analysis was conducted using EDX detector (X-max 80, Oxford Instruments plc). The powder XRD pattern was obtained using a Co-source diffractometer (Malvern PANalytical Empyrean, Co-Kα_{1,2} radiation) to identify the phases present in the samples. Magnets were crushed into powder with particle sizes under 100 μm. The diffraction patterns were recorded in a 2θ range of 15° and 90° with an angular step interval of 0.01313°. Rietveld refinement was carried out with the FullProf suite. Lastly, the magnetic domain structures were analyzed using a magneto-optical Kerr microscope (evico magnetics GmbH) with polar sensitivity.

Supporting Information

Supporting Information is available from the Wiley Online Library or from the author.

Acknowledgements

The work thanks the German Ministry of Education and Research, Project “Scale2PM” (Skalierung der 2-Pulvermethode zur Herstellung von Permanentmagneten mit reduziertem Gehalt kritischer Elemente) [grant no. 03VP10552], and the Deutsche Forschungsgemeinschaft (DFG, German Research Foundation), Project ID No. 405553726, TRR 270 for financial support.

Open Access funding enabled and organized by Projekt DEAL.

Conflict of Interest

The authors declare no conflict of interest.

Author Contributions

Chi-Chia Lin: conceptualization (lead); funding acquisition (supporting); investigation (lead); methodology (lead); project administration (supporting); validation (lead); visualization (lead); writing—original draft (lead).
Konrad Opelt: conceptualization (supporting); funding acquisition (lead); investigation (supporting); project administration (lead); validation

(supporting); writing—review & editing (supporting). **Jürgen Dieter Rossa**: investigation (supporting); methodology (supporting); validation (supporting). **Fernando Maccari**: investigation (supporting); methodology (supporting); writing—original draft (supporting). **Songhak Yoon**: investigation (supporting); methodology (supporting); software (lead); writing—original draft (supporting). **Jürgen Gassmann**: funding acquisition (equal); project administration (supporting); supervision (supporting); writing—review & editing (supporting). **Oliver Gutfleisch**: methodology (supporting); project administration (supporting); supervision (equal); validation (supporting); writing—review & editing (lead).

Data Availability Statement

Research data are not shared.

Keywords

cerium, core-shell structures, criticality, permanent magnets, processing technology, rare-earth

Received: January 6, 2025
Revised: March 24, 2025
Published online: May 13, 2025

- [1] O. Gutfleisch, M. A. Willard, E. Brück, C. H. Chen, S. G. Sankar, J. P. Liu, *Adv. Mater.* **2011**, 23, 821.
- [2] Supply and Demand, <https://www.arultd.com/products/supply-and-demand> (accessed: March 2024).
- [3] J. M. D. Coey, *Engineering* **2020**, 6, 119.
- [4] *Rare Earth Market Outlook to 2035*, Adamas Intelligence **2022**.
- [5] K.-H. Müller, S. Sawatzki, R. Gauß, O. Gutfleisch, *Permanent Magnet Materials and Applications* **2021**, Springer, Cham, 1369. https://doi.org/10.1007/978-3-030-63210-6_29.
- [6] K. Binnemans, P. T. Jones, T. Müller, L. Yurramendi, *J. Sustainable Metall.* **2018**, 4, 126.
- [7] J. M. D. Coey, *Scr. Mater.* **2012**, 67, 524.
- [8] K. P. Skokov, O. Gutfleisch, *Scr. Mater.* **2018**, 154, 289.
- [9] J. F. Herbst, *Rev. Mod. Phys.* **1991**, 63, 819.
- [10] C. Yan, S. Guo, R. Chen, D. Lee, A. Yan, *IEEE Trans. Magn.* **2014**, 50, 1. <https://doi.org/10.1109/TMAG.2014.2322823>.
- [11] J. F. Herbst, M. S. Meyer, F. E. Pinkerton, *J. Appl. Phys.* **2012**, 111, 7.
- [12] A. Alam, M. Khan, R. W. McCallum, D. D. Johnson, *Appl. Phys. Lett.* **2013**, 102, 4.
- [13] E. Niu, Z.-A. Chen, G.-A. Chen, Y.-G. Zhao, J. Zhang, X.-L. Rao, B.-P. Hu, Z.-X. Wang, *J. Appl. Phys.* **2014**, 115, 11.
- [14] L. Paolasini, P. Dervenagas, P. Vulliet, J.-P. Sanchez, G. H. Lander, A. Hiess, A. Panchula, P. Canfield, *Phys. Rev. B* **1998**, 58, 12117.
- [15] Y. Zhang, T. Ma, J. Jin, J. Li, C. Wu, B. Shen, M. Yan, *Acta Mater.* **2017**, 128, 22.
- [16] C. Meyer, F. Hartmann-Boutron, Y. Gros, Y. Berthier, J. Buevoz, *J. Phys.* **1981**, 42, 605.
- [17] C. C. Tang, W. S. Zhan, Y. X. Li, D. F. Chen, J. Du, G. H. Wu, Z. W. Gan, S. R. Qi, *J. Phys. D: Appl. Phys.* **1998**, 31, 2426.
- [18] Y. C. Chuang, C. H. Wu, Z. B. Shao, *J. Less-Common Met.* **1987**, 136, 147.
- [19] K. D. Durst, H. Kronmüller, *J. Magn. Magn. Mater.* **1987**, 68, 63.
- [20] T. G. Woodcock, Y. Zhang, G. Hrkac, G. Ciuta, N. M. Dempsey, T. Schrefl, O. Gutfleisch, D. Givord, *Scr. Mater.* **2012**, 67, 536.
- [21] K. Hono, H. Sepehri-Amin, *Scr. Mater.* **2012**, 67, 530.
- [22] K. Chen, S. Guo, X. Fan, G. Ding, J. Di, R. J. Chen, D. Lee, A. Yan, *AIP Adv.* **2017**, 7, 2.
- [23] F. Xia, Q. Sun, M. Zhu, Y. Wang, Y. Fang, W. Li, *Mater. Des.* **2022**, 216, 110590.
- [24] T. Ma, M. Yan, K. Wu, B. Wu, X. Liu, X. Wang, Z. Qian, C. Wu, W. Xia, *Acta Mater.* **2018**, 142, 18.
- [25] J. Jin, M. Yan, W. Chen, W. Zhang, Z. Zhang, L. Zhao, G. Bai, J. Grenèche, *Acta Mater.* **2021**, 204, 116529.
- [26] J. Jin, Y. Tao, X. Wang, Z. Qian, W. Chen, C. Wu, M. Yan, *J. Mater. Sci. Technol.* **2022**, 110, 239.
- [27] M. Tang, X. Bao, K. Lu, L. Sun, X. Mu, J. Li, X. Gao, *J. Magn. Magn. Mater.* **2017**, 442, 338.
- [28] J. Wang, G. Wang, D. Zeng, *J. Magn. Magn. Mater.* **2020**, 503, 166639.
- [29] F. Chen, M. Cong, H. Chen, N. Liu, D. Wang, X. Wang, Y. Zhao, W. Zhao, *J. Alloys Compd.* **2020**, 819, 152965.
- [30] Q. Zhu, Y. Lin, Z. Ma, W. Li, S. Zhang, B. Zheng, C. Xu, L. Yang, H. Li, *J. Magn. Magn. Mater.* **2020**, 515, 167274.
- [31] R. Du, R. Chen, G. Ding, X. Fan, X. Tang, S. Cao, S. Guo, A. Yan, X. Liu, *J. Magn. Magn. Mater.* **2022**, 551, 169034.
- [32] M. Zhu, W. Li, J. Wang, L. Zheng, Y. Li, K. Zhang, H. Feng, T. Liu, *IEEE Trans. Magn.* **2014**, 50, 1. <http://doi.org/10.1109/TMAG.2013.2278018>.
- [33] M. Zhu, R. Han, W. Li, S. Huang, D. Zheng, L. Song, X. Shi, *IEEE Trans. Magn.* **2015**, 51, 1. <https://doi.org/10.1109/TMAG.2015.2451696>.
- [34] X. Fan, S. Guo, K. Chen, R. Chen, D. Lee, C. You, A. Yan, *J. Magn. Magn. Mater.* **2016**, 419, 394.
- [35] Y. Zhang, T. Ma, M. Yan, J. Jin, B. Wu, B. Peng, Y. Liu, M. Yue, C. Liu, *Acta Mater.* **2018**, 146, 97.
- [36] J. Jin, M. Yan, Y. Liu, B. Peng, G. Bai, *Acta Mater.* **2019**, 169, 248.
- [37] G. Delette, *J. Magn. Magn. Mater.* **2023**, 577, 170768.
- [38] G. Hrkac, T. G. Woodcock, K. T. Butler, L. Saharan, M. T. Bryan, T. Schrefl, O. Gutfleisch, *Scr. Mater.* **2014**, 70, 35.
- [39] H. Nakamura, K. Hirota, T. Ohashi, T. Minowa, *J. Phys. D: Appl. Phys.* **2011**, 44, 064003.
- [40] K. Löwe, C. Brombacher, M. Katter, O. Gutfleisch, *Acta Mater.* **2015**, 83, 248.
- [41] Z. W. Liu, J. Y. He, R. V. Ramanujan, *Mater. Des.* **2021**, 209, 110004.
- [42] K. Löwe, W. Fernengel, K. Skokov, O. Gutfleisch, *WO/2016/180912*, **2016**.
- [43] K. Opelt, T. Ahmad, O. Diehl, M. Schönfeldt, E. Brouwer, I. Vogel, J. D. Rossa, J. Gassmann, S. Ener, O. Gutfleisch, *Adv. Eng. Mater.* **2021**, 23, 2100459.
- [44] R. M. German, P. Suri, S. J. Park, *J. Mater. Sci.* **2009**, 44, 1. <https://doi.org/10.1007/s10853-008-3008-0>.
- [45] K. Opelt, C.-C. Lin, M. Schönfeldt, J. Gassmann, S. Yoon, O. Gutfleisch, *Acta Mater.* **2024**, 270, 119871.
- [46] H. Kronmüller, *Phys. Status Solidi B* **1987**, 144, 385.
- [47] H. Kronmüller, K. D. Durst, S. Hock, G. Martinek, *J. Phys. Colloq.* **1988**, 49, 623.
- [48] M. Sagawa, S. Hirosawa, H. Yamamoto, S. Fujimura, Y. Matsuura, *Jpn. J. Appl. Phys.* **1987**, 26, 785.
- [49] C. C. Tang, W. S. Zhan, Y. X. Li, D. F. Chen, J. Du, G. H. Wu, J. Y. Li, K. C. Jia, *J. Phys.: Condens. Matter* **1997**, 9, 9651.
- [50] A. Hubert, R. Schäfer, *Magnetic Domains*, Springer Berlin, Heidelberg **1998**.
- [51] D. Goll, R. B. Loeffler, J. F. Herbst, R. Karimi, G. Schneider, *J. Phys.: Condens. Matter* **2014**, 26, 064208.
- [52] R. Bodenberger, A. Hubert, *Phys. Status Solidi A* **1977**, 44, K7.
- [53] Rare Earths, <https://mineralprices.com/rare-earths/> (accessed: March 2024).